

# **Inter-Hemispheric Influence of the Atlantic Warm Pool on the Southeastern Pacific**

Chunzai Wang<sup>1</sup>

Sang-Ki Lee<sup>2</sup>

Carlos R. Mechoso<sup>3</sup>

<sup>1</sup> NOAA Atlantic Oceanographic and Meteorological Laboratory  
Miami, Florida

<sup>2</sup> Cooperative Institute for Marine and Atmospheric Studies  
University of Miami  
Miami, Florida

<sup>3</sup> University of California, Los Angeles  
Los Angeles, California

Revised to *Journal of Climate*

June 2009

Corresponding author address: Dr. Chunzai Wang, NOAA/AOML, Physical Oceanography Division, 4301 Rickenbacker Causeway, Miami, FL 33149.  
E-mail: Chunzai.Wang@noaa.gov.

## **Abstract**

The Atlantic warm pool (AWP) is a large body of warm water comprising the Gulf of Mexico, Caribbean Sea, and western tropical North Atlantic. The AWP can vary on seasonal, interannual, and multidecadal timescales. The maximum AWP size is in the boreal late summer and early fall, with the largest extent in the year being about three times the smallest one. The AWP alternates with the Amazon basin in South America as the seasonal heating source for circulations of the Hadley and Walker type in the Western Hemisphere. During the boreal summer/fall, a strong Hadley-type circulation is established, with ascending motion over the AWP and subsidence over the southeastern tropical Pacific. This is accompanied by equatorward flow in the lower troposphere over the southeastern tropical Pacific, as dynamically required by the Sverdrup vorticity balance.

It is shown by analyses of observational data and NCAR community atmospheric model simulations that an anomalously large (small) AWP during the boreal summer/fall results in a strengthening (weakening) of the Hadley-type circulation with enhanced descent (ascent) over the southeastern tropical Pacific. It is further demonstrated – by using a simple two-level model linearized about a specified background mean state – that the inter-hemispheric connection between the AWP and the southeastern tropical Pacific depends on the configuration of the background mean zonal winds in the Southern Hemisphere.

## 1. Introduction

The southeastern tropical Pacific (SEP) is characterized by large-scale subsidence, extensive and persistent stratocumulus clouds, and cold sea surface temperatures (SSTs). Under the subsidence, surface winds evaporate water vapor from the ocean, but the atmospheric inversion prevents the moist air from rising to significant elevations. A thin layer of stratus or stratocumulus clouds forms at the base of the inversion and shield the ocean surface from solar radiation. Light precipitation (drizzle) under the stratus cloud deck is a prominent regional feature, which is directly influenced by subsidence (e.g., Wang et al. 2004). The cold SSTs, light precipitation, and extensive stratocumulus cloud cover in the SEP are all integral parts of the inter-hemispheric asymmetry of the eastern tropical Pacific climate (e.g., Philander et al. 1996; Ma et al. 1996; Yu and Mechoso 1999).

The subtropical high in the South Pacific and subsidence over the SEP during the austral summer (boreal winter) are related to the monsoonal heating over South America. Rodwell and Hoskins (2001) demonstrate by using an atmospheric model that Rossby wave response to heating associated with the South American monsoon system interacting with the midlatitude westerlies produces descending motion to the west of the South American heating, i.e., over the SEP. The Sverdrup balance demands the existence of equatorward flow beneath the region of descent, closing off the South Pacific subtropical anticyclone on its eastern flank. During seasons other than the austral summer, when convective activity over South America is weaker, other processes must be responsible for maintaining the subsidence over the SEP. Richter and Mechoso (2008) demonstrate that the westerly wind impinging on the Andes mountains contributes to sinking along the equatorward sloping isentropes thus promoting subsidence over

the SEP. This process must be at work in all seasons, but the effects would be primarily confined near the coastal region.

In the Western Hemisphere during the boreal summer/fall, diabatic heating is the largest over the region of the Western Hemisphere warm pool (WHWP; Wang and Enfield 2001, 2003). This region alternates with northern South America as the seasonal heating source for the Walker and Hadley-type circulations in the Western Hemisphere. The Central America landmass divides the WHWP into two ocean regions: the eastern North Pacific warm pool in the west and the Atlantic warm pool (AWP) in the east. As shown by Wang et al. (2006), an anomaly index of the eastern North Pacific warm pool extent is highly correlated with ENSO as expected by the closeness between the two regions. Since here we are interested in non-ENSO influences on climate, we focus on the AWP component of the WHWP.

The AWP is a large body of warm water comprising the Gulf of Mexico, Caribbean Sea, and western tropical North Atlantic. In extent, the AWP varies on seasonal, interannual, and multidecadal timescales with maximum size in the boreal summer/fall that is almost three times the smallest one (Wang et al. 2008b). During the season of maximum extent, a strong Hadley-type circulation is established with ascending branch near the AWP and subsidence over the SEP. Analyses of observational data have shown that an index representative of the anomalous warm pool extent is positively correlated with rainfall anomalies over the SEP (Wang et al. 2006), where drizzle (light precipitation) usually appears under the stratus cloud deck. The links between the warm pool and the SEP are set through the regional Hadley-type circulation: an anomalously large (small) warm pool during the boreal summer/fall strengthens (weakens) the Hadley ascent in the region and associated subsidence over the SEP. Such anomalies impact regional stratus cloud incidence and drizzle in the region. Wang et al. (2006) also show that

ENSO and other local SST anomalies contribute little to the positive correlation between the AWP index and rainfall anomalies over the SEP.

Our objective in the present paper is to describe the inter-hemispheric influences of the AWP on the SEP, and to demonstrate how such influences are established. We use both an atmospheric general circulation model (AGCM) and a simple atmospheric model to investigate the AWP's remote and inter-hemispheric effects on the SEP during the boreal summer and fall. Section 2 describes the datasets and models used in this study. Section 3 presents a summary of the associations between anomalies in the AWP and the atmospheric circulation as evidenced by observational data. Sections 4 and 5 present the results obtained with the AGCM and the simple atmospheric model, respectively. Section 6 provides a discussion and summary.

## **2. Datasets and models**

Two datasets are used in this study. The first is the updated National Center for Environmental Prediction-National Center for Atmospheric Research (NCEP-NCAR) reanalysis from January 1949 to December 2006, which is available on a  $2.5^\circ$  latitude by  $2.5^\circ$  longitude grid (Kalnay et al. 1996). The second dataset is the Hadley Centre Sea Ice and SST dataset (HadISST) from 1949 to 2006; this is available on a  $1^\circ$  latitude by  $1^\circ$  longitude resolution (Rayner et al. 2003). Anomaly fields are calculated by subtracting the monthly climatologies from the total data.

We use two numerical models of the atmosphere. The more complex one is the latest version (version 3.1) of the NCAR community atmospheric model (CAM3). This is a global spectral model with triangular spectral truncation of the spherical harmonics at zonal wave number 42 (T42), which roughly gives a  $2.8^\circ$  latitude by  $2.8^\circ$  longitude horizontal resolution. In

the vertical, the domain is divided into 26 hybrid sigma-pressure layers. The vertical finite differencing is based on the pressure coordinate in the upper regions of the atmosphere, sigma coordinate in the lower troposphere, and a hybrid pressure-sigma coordinate in the middle levels. The reader is referred to Collins et al. (2006) for more detailed information on the physical parameterizations of CAM3, and to Hurrell et al. (2006) and Deser et al. (2006) for an assessment of the model's performance on seasonal variations and interannual variability.

The monthly distributions of SST prescribed in CAM3 are obtained from the HadISST dataset (Rayner et al. 2003). As described in Wang et al. (2008a), three sets of ensemble model simulations (with 20 year run) are conducted: 1) control (CTRL), 2) large AWP (LAWP), and 3) small AWP (SAWP). In CTRL, CAM3 uses monthly mean climatological SST globally. In LAWP, the monthly-mean SSTs correspond to the large AWP composites in the region from 5°N to 30°N between 40°W and the coast of the Americas and to the climatology elsewhere. In SAWP, the prescribed SSTs correspond to the small AWP composites, while the climatology is prescribed elsewhere. To minimize discontinuities in the SST distribution around the edges of the AWP domain, we apply a smoothing to the five model grids centered at the boundary with weights of 1.0, 0.75, 0.50, 0.25, and 0.0 from inside to outside the region. In order to highlight the effects of the anomalous AWP, we will examine the differences between the LAWP and SAWP runs (LAWP minus SAWP). For additional details on model design and associated SST distributions, the reader is referred to Wang et al. (2008a).

To gain insight into on the local and remote responses to tropical heating anomalies associated with the AWP, we also use a simple atmospheric model developed recently by Lee et al. (2009). This is a steady-state two-level primitive equation model, linearized about a prescribed background mean state. The formulation is similar to that of the multilevel linear

baroclinic model used by Hoskins and Simmons (1975) and others, but its governing equations are greatly simplified by employing Gill's (1980) simple thermodynamic equation (see Appendix for a brief description of the simple model). The simple model captures three fundamental dynamic processes: (1) a heat-induced baroclinic mode as described by the Matsuno-Gill model (Matsuno 1966; Gill 1980); (2) a barotropic Rossby wave source resulting from conversion of the heat-induced baroclinic mode into barotropic anomalies; and (3) teleconnections to high latitudes, as in the barotropic stationary wave model of Branstator (1983). Using the model, Lee et al. (2009) show that background vertical zonal wind shear by interacting with heat-induced baroclinic flow anomalies produces barotropic motions near the heating source. These barotropic flow anomalies in turn interact with the height-independent mean westerly wind to transmit the barotropic signals to high latitudes and other ocean basins. The background mean wind fields therefore play important roles on the barotropic teleconnections between tropical heating and high latitudes. Model parameters used in the present study are the same as those in Lee et al. (2009), except for a barotropic linear damping coefficient of  $(10 \text{ days})^{-1}$  and a barotropic horizontal mixing coefficient of  $2.5 \times 10^5 \text{ m}^2/\text{s}$ .

### **3. Observational results**

Several papers have documented the AWP variability and its associated atmospheric circulation anomalies based on observational data (Wang and Enfield 2001 and 2003; Wang et al. 2006 and 2008b). For convenience and continuity, here we briefly present selected features. Also, we refer to the winter as the period from December to February (DJF), the spring from March to May (MAM), the summer from June to August (JJA), and the fall from September to November (SON).

The seasonal-mean SSTs near the AWP region are shown in Fig. 1. Wang and Enfield (2001, 2003) defined the warm pool as the region covered by water warmer than  $28.5^{\circ}\text{C}$ . This value was chosen because it represents the threshold for large-scale deep tropospheric convection (e.g., Graham and Barnett 1987). In addition, the depth of the  $28.5^{\circ}\text{C}$  isotherm is close to the average mixed layer depth in the AWP (Wang and Enfield 2003). As shown in Figs. 1a and 1b, the SST in the Gulf of Mexico and the Caribbean Sea is mostly below  $27.5^{\circ}\text{C}$  during DJF and MAM. By JJA, SSTs in the Gulf of Mexico and region surrounding Cuba are warmer than  $28.5^{\circ}\text{C}$  (Fig. 1c). During SON, the warm pool expands south into the Caribbean Sea and eastward into the western tropical North Atlantic, while the water in the Gulf of Mexico cools down (Fig. 1d). Wang and Enfield (2001 and 2003) give a detailed description of the SST seasonal cycle and associated subsurface temperature variations in the AWP, and Lee et al. (2007) attempt a better understanding of associated physical processes by using an ocean general circulation model.

Figure 2 presents the seasonal-mean velocity potential and divergent wind at 200-mb over the globe. The largest warm pool in the western Pacific is associated with the strongest divergent outflows in the upper troposphere, and has been extensively studied in association with ENSO (e.g., Webster and Lukas 1992). The AWP in the Western Hemisphere is the second largest warm pool. During the boreal winter, the heat source in the Western Hemisphere is associated with the South American monsoon system. Ascending motion over the Amazon heat source produces upper tropospheric divergence over South America (Fig. 2a). The regions of associated subsidence are over the subtropical North Atlantic, South Atlantic, and southeast Pacific, i.e., over the subtropical highs in the North and South Atlantic, and the South Pacific (e.g., Rodwell and Hoskins 2001; Richter and Mechoso 2008). During the spring (MAM), the



center of tropospheric heating and convection shifts from the Amazon toward the equator (Fig. 2b). In the summer (JJA), the center of tropospheric heating and convection completely shifts to the AWP region (Fig. 2c). Thus, in this season, a Hadley-type circulation is established with ascent over the AWP and subsidence over the subtropical South Atlantic and South Pacific (Fig. 2c). This Hadley-type circulation persists until the beginning of the fall (Fig. 2d).

The AWP also shows a strong interannual variability (Wang et al. 2006; Wang et al. 2008b). The influence of this variability on the SEP can be examined by compositing distributions corresponding to large and small AWP years. Using the HadISST dataset, we first calculate an anomalous AWP index defined as the area covered by SSTs warmer than 28.5°C during June-October. Wang et al. (2006 and 2008b) show that the AWP index defined in this way is not contemporaneously correlated with ENSO. A warm pool with an area 25% larger (smaller) than the climatological one is identified as a large (small) AWP; otherwise, warm pools are labeled as normal or neutral. Next we calculate the composite difference between the large and small AWP years (LAWP – SAWP) of the velocity potential and divergent wind at 200-mb from the NCEP-NCAR reanalysis (see Fig. 3). As shown in Wang et al. (2006), the anomalous size of the AWP changes little during the winter/spring and its associated influence on the atmosphere is small during that time. Therefore, here we only discuss anomalous influence of the AWP during the summer and fall. Figure 3 shows that the anomalous AWP during those seasons are associated with divergent flow of the upper troposphere that crosses the equator into the southeast Pacific. That is, the anomalous Hadley-type circulation shows ascent west of the AWP and descent over the SEP. In view of the mean circulation pattern in the seasons considered (Figs. 2c and 2d), the effect of the anomalous AWP is to strengthen the regional Hadley-type circulation from the AWP region to the SEP. This meridional circulation reinforces

the South Pacific subtropical anticyclone and strengthens easterly trade winds near the equatorial eastern/central Pacific. The strengthened easterly trade winds can cool the equatorial eastern Pacific Ocean and thus may play a role in the initiation of a cool phase of ENSO.

#### **4. CAM3 results**

Wang et al. (2007) compared the CAM3 model simulation of the AWP with the NCEP-NCAR reanalysis fields and the Climate Prediction Center merged analysis of precipitation. Here we focus on the simulated mechanism for the AWP's impact on the SEP. CAM3 captures the direct-type atmospheric circulation pattern established between these regions (Fig. 4). In comparison with the NCEP-NCAR reanalysis (Fig. 2), CAM3 does a reasonably good job in simulating the seasonal atmospheric circulation pattern. As shown in Figs. 4a and 4b, a center of upper tropospheric divergence is located over South America during the boreal winter and spring. As the season progresses, the center location is over the AWP, where SSTs are high in the summer and fall (Figs. 4c and 4d and Figs. 1c and 1d). During that time of a year, the divergent flow of the upper troposphere from the AWP crosses the equator, converges over the SEP, and thus feeds and/or maintains local subsidence over the South Pacific subtropical high.

The impact of the anomalous AWP on the SEP can be obtained by inspection of the difference between the model runs of LAWP and SAWP (i.e., LAWP – SAWP). The differences in velocity potential and divergent wind at 200-mb during the summer and fall are shown in Figs. 5a and 5b, respectively. CAM3 captures inter-hemispheric influence feature of the anomalous AWP on the SEP by showing cross-equatorial flow southward from the AWP to the SEP, where the flow converges and descends and the South Pacific subtropical high intensifies. However, a comparison of Fig. 5 with Fig. 3 shows some differences between the model runs and NCEP-

NCAR reanalysis. First, the CAM3 simulated influence pattern of the AWP on the SEP, i.e., the velocity potential centers in the AWP and SEP and the divergent flow from the AWP to the SEP, is larger than that from the NCEP-NCAR reanalysis. Second, the negative center of velocity potential during JJA from the NCEP-NCAR reanalysis is in the west coast of North Africa (Fig. 3a), whereas the center of simulated velocity potential during JJA is in the western Indian Ocean (Fig. 4a). These discrepancies between simulation and observation may be attributed to many factors. For example, the composites from the NCEP-NCAR reanalysis (i.e., Fig. 3) are calculated as the average differences between large and small AWP years, which also include the effects of other variabilities in regions such as the tropical eastern North Atlantic and Africa. However, the CAM3 model runs only consider the influences associated with variability in the circulations due to AWP-heating. Since we are primarily interested in the mechanisms for AWP influence on the SEP, we believe that discrepancies between the simulation and NCEP-NCAR reanalysis will not challenge our conclusions.

To visualize further how the AWP variability affects SEP subsidence, we plot longitude-height sections of vertical pressure velocity at 25°S during the austral winter and spring in Figs. 6 and 7, respectively. According to Figs. 6a and 7a, the descending motion over the SEP maximizes in the lower troposphere, where low-level clouds form at the base of the atmospheric inversion. The vertical velocity differences in LAWP – SAWP in Figs. 6b and 7b show descending motion over a broad area of the SEP, with strongest values around 110°W and 400-mb. Ascending motion is seen over South America. Therefore, an anomalously large (small) AWP has an inter-hemispheric impact by strengthening (weakening) subsidence over the SEP and ascent over South America.

The descending and ascending motions described above are dynamically consistent with the Sverdrup vorticity balance (e.g., Hoskins 1996; Rodwell and Hoskins 2001; Seager et al. 2003; Nigam and Ruiz-Barradas 2006):  $\beta v = f \partial w / \partial z = -f \nabla \cdot \vec{u}$ , where  $\beta$  is the planetary vorticity gradient and  $f$  is the Coriolis parameter. The Sverdrup balance requires descent (ascent) to be accompanied by equatorward (poleward) from the level of maximum vertical velocity (i.e., from the level of  $\partial w / \partial z = 0$ ) to the surface. This relationship is held in the model runs of both CTRL and LAWP – SAWP. Figures 6 and 7 show equatorward flows at 25°S over the SEP below the level of maximum descending motion for the seasonal and anomalous AWP cases. This indicates that the Sverdrup balance is operating on CAM3 model runs.

There are both local and remote atmospheric responses to the AWP variability. As will be shown in Section 5, a local heat-induced atmospheric response is better represented by the baroclinic stream function, whereas teleconnected pattern to high latitudes and other ocean basins can be captured by the barotropic stream function. For a close examination of these responses, it therefore is useful to separate the model solutions into their baroclinic and barotropic components. For consistency with the simple model results shown in the following section, the baroclinic and barotropic stream functions in the CAM3 runs are calculated as  $\hat{\psi} = (\psi_{750mb} - \psi_{250mb}) / 2$  and  $\bar{\psi} = (\psi_{750mb} + \psi_{250mb}) / 2$ , respectively. Figure 8 shows the differences of the baroclinic and barotropic stream functions in LAWP – SAWP during the boreal summer and fall. For both the seasons, the baroclinic stream function shows a pair of cyclones: one in the northeast Pacific and the other in the SEP (Figs. 8a and 8c). This model response is largely consistent with Gill's (1980) solution to a heating anomaly slightly north of the equator (Heckley and Gill 1984). The barotropic stream functions are shown in Figs. 8b and 8d. Over the SEP, the barotropic anticyclone tends to weaken (enhance) the baroclinic cyclone

(anticyclone) in the lower (upper) troposphere. In this way, the cyclonic stream function anomalies of the lower troposphere are weakened, whereas those in the upper troposphere are strengthened (Fig. 9). The AWP's teleconnection in the fall is stronger than that in the summer. This can be partly due to the largest SST anomalies in the AWP during the boreal fall.

## 5. Simple model results

In this section we use the model developed by Lee et al (2009) to gain insight into the way in which connections are established between the AWP and the SEP, as observed and simulated by CAM3 in Sections 3 and 4, respectively. The results obtained demonstrate the crucial role played by background zonal flow in the propagation of tropical heat-induced anomalies to high latitudes. The background vertical zonal wind shear (or the background baroclinic zonal wind component) produces barotropic motions near the heating source, which can in turn propagate to high latitudes in the presence of barotropic background westerly winds (i.e., height-independent background westerly winds). The background mean states prescribed in this study correspond to zonal averages between 120°W-40°W during JJA and SON from the NCEP-NCAR reanalysis (see Fig. 10). The background baroclinic and the barotropic zonal winds are defined as  $\hat{U} = (U_{750mb} - U_{250mb}) / 2$  and  $\bar{U} = (U_{750mb} + U_{250mb}) / 2$ , respectively. Both the background vertical wind shear and height-averaged wind are stronger in the Southern Hemisphere during the boreal summer (see also Peixoto and Oort 1992). A Gaussian-shaped heating anomaly is prescribed in the AWP region with center around (70°W, 15°N).

The model results for the baroclinic and barotropic stream functions during the boreal summer and fall are shown in Figs. 11 and 12, respectively. The atmospheric response to the AWP heating anomaly is similar in the two seasons considered, as expected since the differences

between the background mean states are relatively small (Fig. 10). As in the CAM3 simulation (see Fig. 8 and Wang et al. 2008a), the baroclinic stream functions from the simple model show a pair of cyclones in the northeast Pacific and the SEP (Figs. 11a and 12a). This pattern is indicative that Gill's dynamics is at work with the heating anomaly at 15°N producing a westerly wind anomaly south of the heat source. The pattern is also consistent with the results of Heckely and Gill (1984), who showed that a heating anomaly slightly north of the equator produces a pair of cyclones north and south of the equator in Gill's model (1980). The barotropic component of the response shows a pattern of alternating high and low centers from the AWP region to high latitudes (Figs. 11b and 12b). In particular, the AWP heat-induced stream function crosses the equator into high latitudes of the Southern Hemisphere, in a way consistent with the CAM3 results shown in Fig. 8b and 8d.

As stated earlier, the background mean zonal winds are important for the propagation of heat-induced signals from tropics to high latitudes. In particular, teleconnections between the AWP and the Southern Hemisphere are larger in the austral winter (Fig. 11b) when both the background vertical wind shear and height-averaged wind are stronger during that time over the Southern Hemisphere (Peixoto and Oort 1992). To further examine the effect of background mean states on inter-hemispheric teleconnections, we perform two additional model experiments with either no baroclinic or barotropic mean zonal flow (i.e.,  $\hat{U} = 0$ ,  $\bar{U} = 0$ ) over the Southern Hemisphere. Figures 13 and 14 show the results of these two model experiments. Comparisons of Figs. 13 and 14 with Fig. 11 show that the baroclinic stream functions for the cases with zero background mean zonal winds (i.e.  $\hat{U} = 0$  and  $\bar{U} = 0$ ) over the Southern Hemisphere are practically identical. The local baroclinic response to the AWP heating, therefore, is largely independent of the background mean zonal winds (Lee et al. 2009). Gill's (1980) model, for

example, does not include a background mean state in its governing equations but it still can simulate basic features of baroclinic response associated with ENSO (Zebiak 1986). In contrast, the background mean zonal winds play a key role for the barotropic stream function to propagate into the Southern Hemisphere. For example, if  $\hat{U} = 0$  the barotropic stream function is practically zero in the Southern Hemisphere (Fig. 13b). In this case, the AWP heat-induced baroclinic anomalies cannot interact with the background vertical wind shear to produce barotropic motion in the Southern Hemisphere. In addition, if  $\bar{U} = 0$  the barotropic stream function in the Southern Hemisphere is much weaker and does not propagate to high latitudes (Fig. 14b). Therefore, the simple model results suggest that the background westerly winds in the Southern Hemisphere are important for the AWP heat-induced signals to transmit to high latitudes of the Southern Hemisphere.

## 6. Summary and discussion

Over the Western Hemisphere, two large heating centers are dominant: Amazonia and the Western Hemisphere warm pool (WHWP). The relative importance of these two heating centers alternates with season. When the sun is over the Southern Hemisphere during the austral summer, diabatic heating associated with Amazonian convection induces divergent flows in the upper troposphere that flow westward and eastward to maintain the subsidence and anticyclones in the southeast Pacific and South Atlantic, respectively. As argued by Rodwell and Hoskins (2001), the austral summer monsoonal heating over South America is associated with subsidence over the southeastern tropical Pacific (SEP). During that time, the Amazonian convection activity also provides a cross-hemispheric connection to the North Atlantic subtropical high north at around 20°N via a regional Hadley-type circulation (Wang 2002). When the season

progresses with the sun transiting toward the Northern Hemisphere, the heating source also transits to the WHWP region. In the boreal summer, the heating source is over the warm pool region inducing divergent outflows in the upper troposphere. These divergent flows cross the equator, reach/converge in the SEP and sustain/feed the subsidence over there. Therefore, during the boreal summer when Amazonian convection is weaker, WHWP heating maintains the subsidence over the SEP, thus establishing an inter-hemispheric link through a Hadley-type circulation.

The paradigm just described also applies to the inter-hemispheric influence of anomaly in tropical heating fields. The present paper mainly focuses on the influence of anomalies in the AWP since the eastern North Pacific warm pool (the other part of the WHWP) is highly correlated with ENSO and therefore belongs in a different context. The NCEP-NCAR reanalysis shows that an anomalously large (small) AWP is associated with stronger (weaker) regional Hadley-type circulation emanating from the AWP region in the upper troposphere into the SEP where the anomalous convergence (divergence) is located. Wang et al. (2006) further showed that these convergence and divergence in the upper troposphere correspond to the anomalous descent and ascent at 500-mb over the SEP, respectively. A larger (smaller) AWP is observed to strengthen (weaken) the seasonal subsidence over the SEP through strengthening (weakening) of the Hadley-type circulation.

Ensemble runs by CAM3 basically capture the inter-hemispheric influence feature of the AWP on the SEP on both seasonal and anomalous variations. The simulated impacts of seasonal and anomalous variations of the AWP show that heating in this region produces local divergence in the upper troposphere and air flows across the equator into the SEP, where it converges and descends. This simulated subsidence over the SEP is accompanied by equatorward flow in the



lower troposphere, as dynamically required by the Sverdrup vorticity balance. The equatorward wind along the west coast of South America and associated surface wind stresses lead to Ekman transport and pumping that can cool the SSTs and enhance coastal upwelling. The possibility of such processes needs to be addressed by using coupled ocean-atmosphere models.

The inter-hemispheric influence of the AWP on the SEP is further examined by using a simple atmospheric model. The model is linearized about a background mean state (see Appendix for a brief model description), and can simulate both local and remote responses to tropical heating anomalies (Lee et al. 2009). The simple model results show that interaction between the AWP heat-induced anomalies and the atmospheric background mean states is important for the establishment of inter-hemispheric influences. In response to heating anomalies over the AWP, a pair of baroclinic cyclones is formed in the northeast and southeast Pacific, consistent with the Gill's (1980) solution to a heating anomaly slightly north of the equatorial region (also Heckley and Gill 1984). However, the remote influence of the AWP on the SEP is complicated due to the barotropic component of anomalies. The background vertical wind shear, which is particularly strong in the Southern Hemisphere during the austral winter (boreal summer), plays an important role in inducing a barotropic anticyclone in the SEP. This tends to suppress (enhance) the baroclinic cyclone (anticyclone) in the lower (upper) troposphere. The barotropic anomalies in the SEP in turn interact with the height-independent mean westerly wind to transmit the barotropic signals to high latitudes of the Southern Hemisphere in the form of a barotropic Rossby wave train. Therefore, the background mean zonal wind over the Southern Hemisphere is important for the remote impact of AWP heat-induced anomalies to the SEP.

This paper demonstrates the inter-hemispheric influence of the AWP SST-induced heating on the SEP by using observational data, CAM3 and a simple atmospheric model. The SST anomalies in the AWP can vary due to both local and remote processes (such as climate variability in the Pacific, the Atlantic and others). The relative importance of the local and remote processes in producing the variability of AWP SSTs deserves further study. Regardless, both the CAM3 runs and the simple atmospheric model show that the AWP SST-induced heating has an inter-hemispheric impact on the SEP.

The successful simulation of the SEP climate with numerical models is a very challenging problem. Almost of all state-of-the-art coupled ocean-atmosphere models exhibit serious errors in the form of a severe warm bias in simulated SSTs over the SEP (e.g., Mechoso et al. 1995). The present paper shows that the SEP can be remotely influenced by the AWP variability. This indicates that if models cannot succeed in stimulating the AWP variability, they will also fail at least partially over the SEP. Many state-of-the-art climate models suffer from serious climate drift in the annual cycle of atmosphere-ocean processes in the AWP region. For example, the long-term averaged bias of CCSM3 in the boreal summer shows that the AWP region is characterized by 1-3°C of cold SST bias and up to 5 mm/day of dry bias (i.e., less precipitation) (not shown). Hence, the improved simulation of the AWP is an important topic in climate modeling research.

## Appendix: Simple two-level model for heat-induced atmospheric responses

The simple model of Lee et al. (2009) is used in this study to illustrate the importance of the configuration of atmospheric background mean flow for the inter-hemispheric influence of heating anomalies in the AWP. This model is a steady-state two-level primitive equation model, linearized about a specified background flow. Two levels (i.e., 250 mb and 750 mb) are recast as barotropic and baroclinic modes, respectively:

$$\bar{Y} = (Y_1 + Y_2) / 2, \quad (\text{A1})$$

$$\hat{Y} = (Y_2 - Y_1) / 2. \quad (\text{A2})$$

$Y$  stands for any variable with subscripts 1 and 2 denoting values at the upper (250 mb) and lower (750 mb) levels, respectively. The baroclinic mode equations are greatly simplified by using the so-called weak temperature gradient approximation (i.e., thermal advection is neglected) following Gill (1980). In this study, the background mean flow is purely zonal and varies only in  $y$ -direction. Thus, the barotropic vorticity equation of Lee et al. (2009) can be written as:

$$\bar{U} \frac{\partial \bar{\zeta}}{\partial x} + \left( \beta - \frac{d^2 \bar{U}}{dy^2} \right) \bar{v} = -r_0 \bar{\zeta} + A_0 \nabla^2 \bar{\zeta} + F_{\bar{\zeta}}, \quad (\text{A3})$$

where  $\bar{v}$  denotes the barotropic meridional flow anomaly;  $\bar{U}$  is the barotropic background zonal flow;  $\bar{\zeta}$  is the barotropic relative vorticity anomaly;  $\beta$  is the northward gradient of the vertical planetary vorticity;  $r_0$  is the linear momentum damping coefficient for barotropic mode;  $A_0$  is the momentum diffusion coefficient for barotropic mode.  $F_{\bar{\zeta}}$  is given as

$$F_{\bar{\zeta}} = \hat{v} \frac{d^2 \hat{U}}{dy^2} + \frac{d\hat{U}}{dy} \left( \frac{\partial \hat{u}}{\partial x} + \frac{\partial \hat{v}}{\partial y} \right) - \hat{U} \frac{\partial \hat{\zeta}}{\partial x}, \quad (\text{A4})$$

where  $\hat{u}$  and  $\hat{v}$  denote the baroclinic zonal and meridional flow anomaly components, respectively;  $\hat{U}$  is the baroclinic background zonal flow;  $\hat{\zeta}$  is the baroclinic relative vorticity anomaly.  $F_{\bar{\zeta}}$  represents forcing terms involving the products of the background vertical shear and baroclinic wind anomalies. These very important heat-induced forcing terms that produce barotropic flow anomalies, are collectively referred to as Rossby wave source in the literature (e.g., Sardeshmuku and Hoskin 1988). The barotropic disturbances are, however, remained trapped near the tropical heating source if  $\bar{U} \leq 0$ . The barotropic background westerly wind ( $\bar{U} > 0$ ) is required to radiate the heat-induced barotropic signals to high latitudes [see equation 23 in Lee et al. (2009)].

The baroclinic zonal and meridional momentum equations and thermodynamic equation of Lee et al. (2009) can be rewritten as:

$$\bar{U} \frac{\partial \hat{u}}{\partial x} + \left( \frac{\partial \bar{U}}{\partial y} - f \right) \hat{v} = -\frac{\partial \hat{\phi}}{\partial x} - r_1 \hat{u} + A_1 \nabla^2 \hat{u} + F_{\hat{u}}, \quad (\text{A5})$$

$$\bar{U} \frac{\partial \hat{v}}{\partial x} + f \hat{u} = -\frac{\partial \hat{\phi}}{\partial y} - r_1 \hat{v} + A_1 \nabla^2 \hat{v} + F_{\hat{v}}, \quad (\text{A6})$$

$$\gamma \hat{\phi} + c_g^2 \left( \frac{\partial \hat{u}}{\partial x} + \frac{\partial \hat{v}}{\partial y} \right) = -Q, \quad (\text{A7})$$

where  $\hat{\phi}$  is the baroclinic geopotential anomaly;  $f$  is the Coriolis parameter;  $r_1$  is the linear

momentum damping coefficient for baroclinic mode;  $A_1$  is the momentum diffusion coefficient for baroclinic mode;  $c_g$  is internal gravity wave speed; and  $Q$  is proportional to the mass source (or sink) prescribed at the mid-level, but it should be interpreted as the heat source (or sink). Both  $F_{\hat{u}}$  and  $F_{\hat{v}}$  represent baroclinic forcing terms involving the products of the background wind shear and barotropic wind anomalies:

$$F_{\hat{u}} = \hat{U} \frac{\partial \bar{u}}{\partial x} + \bar{v} \frac{\partial \hat{U}}{\partial y}, \quad (\text{A8})$$

$$F_{\hat{v}} = \hat{U} \frac{\partial \bar{v}}{\partial x}. \quad (\text{A9})$$

With the specified background zonal flows of  $\bar{U}$  and  $\hat{U}$ , we can solve the model equations (A3)–(A9) numerically by expressing the prognostic variables as truncated series of spherical harmonics. Since vectors such as horizontal wind fields have multiple values at the poles, the horizontal wind fields are represented in terms of the vertical component of relative vorticity and horizontal divergence prior to applying the numerical solution method. For more details on the method of solution and model results under idealized and realistic background flows, see Lee et al. (2009).

*Acknowledgments.* We thank reviewers' and editor's comments and suggestions. This work was supported by a grant from National Oceanic and Atmospheric Administration (NOAA) Climate Program Office, the base funding of NOAA Atlantic Oceanographic and Meteorological Laboratory (AOML), National Natural Science Foundation of China (No. 40476017), and the

Chinese Ministry of Education's 111 Project (B07036). The findings and conclusions in this report are those of the author(s) and do not necessarily represent the views of the funding agency.

## References

- Branstator, G., 1983: Horizontal energy propagation in a barotropic atmosphere with meridional and zonal structure. *J. Atmos. Sci.*, **40**, 1689-1708.
- Collins, W. D., P. J. Rasch, B. A. Boville, J. J. Hack, J. R. McCaa, D. L. Williamson and B. P. Briegleb, 2006: The formulation and atmospheric simulation of the Community Atmospheric Model Version 3 (CAM3). *J. Climate*, **19**, 2144-2161.
- Deser, C., A. Capotondi, R. Saravanan, and A. S. Phillips, 2006: Tropical Pacific and Atlantic variability in CCSM3. *J. Climate*, **19**, 2451-2481.
- Enfield, D.B., A.M. Mestas-Nunez, and P.J. Trimble, 2001: The Atlantic Multidecadal Oscillation and its relationship to rainfall and river flows in the continental US. *Geophys. Res. Lett.*, **28**, 2077-2080.
- Gill, A. E., 1980: Some simple solutions for heat-induced tropical circulation. *Quart. J. Roy. Meteor. Soc.*, **106**, 447-462.
- Graham, N. E., and T. P. Barnett, 1987: Sea surface temperature, surface wind divergence, and convection over tropical oceans. *Science*, **238**, 657-659.
- Heckley, W. A., and A. E. Gill, 1984: Some simple analytic solutions to the problems of forced equatorial long waves. *Quart. J. R. Met. Soc.*, **110**, 203-217.
- Hoskins, B. J. and A. J. Simmons, 1975: A multi-layer spectral model and the semi-implicit method. *Quart. J. Roy. Meteor. Soc.*, **103**, 553-567.
- Hoskins, B. J., 1996: On the existence and strength of the summer subtropical anticyclones. *Bull. Amer. Meteor. Soc.*, **77**, 1287-1292.

- Hurrell, J. W., J. J. Hack, A. S. Phillips, J. Caron, and J. Yin, 2006: The dynamical simulation of the Community Atmospheric Model Version 3 (CAM3). *J. Climate*, **19**, 2162-2183.
- Kalnay, E., and Co-authors, 1996: The NCEP/NCAR 40-year reanalysis project. *Bull. Am. Meteorol. Soc.*, **77**, 437-471.
- Lee, S. -K., D. B. Enfield, and C. Wang, 2007: What drives seasonal onset and decay of the Western Hemisphere warm pool? *J. Climate*, **20**, 2133-2146.
- Lee, S.-K., C. Wang, and B. Mapes, 2009: A simple atmospheric model of the local and teleconnection responses to heating anomalies. *J. Climate*, **22**, 272-284.
- Ma, C. -C., C. R. Mechoso, A. W. Robertson and A. Arakawa, 1996: Peruvian stratus clouds and the tropical Pacific circulation - a coupled ocean-atmosphere GCM study. *J. Climate*, **9**, 1635-1645.
- Matsuno, T, 1966: Quasi-geostrophic motions in the equatorial area. *J. Meteor. Soc. Japan*, **44**, 25-43.
- Mechoso, C. R., A. W. Robertson, N. Barth, M. K. Davey, P. Delecluse, P. R. Gent, S. Ineson, B. Kirtman, M. Latif, H. Le Treut, T. Nagai, J. D. Neelin, S. G. H. Philander, J. Polcher, P. S. Schopf, T. Stockdale, M. J. Suarez, L. Terray, O. Thual and J. J. Tribbia, 1995: The seasonal cycle over the tropical Pacific in general circulation models. *Mon. Wea. Rev.*, **123**, 2825-2838.
- Nigam, S., and A. Ruiz-Barradas, 2006: Seasonal hydroclimate variability over North America in global and regional reanalysis and AMIP simulations: Varied representation. *J. Climate*, **19**, 815-837.
- Peixoto, J. P., and A. H. Oort, 1992: *Physics of Climate*. American Institute of Physics, New York, 520 pp.



- Philander, S. G. H., D. Gu, D. Halpern, G. Lambert, N. C. Lau, and R. C. Pacanowski, 1996: Why the ITCZ is mostly north of the equator. *J. Climate*, **9**, 2958-2972.
- Rayner, N. A., D. E. Parker, E. B. Horton, C. K. Folland, L. V. Alexander, D. P. Powell, E. C. Kent, and A. Kaplan, 2003: Global analysis of sea surface temperature, sea ice and night marine air temperature since the late nineteenth century. *J. Geophys. Res.*, **108**, 4407, doi:10.1029/2002JD002670.
- Richter, I., and C. R. Mechoso, 2008: What determines the position and intensity of the South Atlantic anticyclone in austral winter? – an AGCM study. *J. Climate*, **21**, 214-229.
- Rodwell, M. J., and B. J. Hoskins, 2001: Subtropical anticyclones and summer monsoons. *J. Climate*, **14**, 3192-3211.
- Sardeshmukh P. D. and B. J. Hoskins, 1988: The generation of global rotational flow by steady idealized tropical divergence. *J. Atmos. Sci.*, **45**, 1228-1251.
- Seager, R., R. Murtugudde, N. Naik, A. Clement, N. Gordon, and J. Miller, 2003: Air-sea interaction and seasonal cycle of the subtropical anticyclones. *J. Climate*, **16**, 1948-1966.
- Wang, C., and D. B. Enfield, 2001: The tropical Western Hemisphere warm pool. *Geophys. Res. Lett.*, **28**, 1635-1638.
- Wang, C., 2002: Atlantic climate variability and its associated atmospheric circulation cells. *J. Climate*, **15**, 1516-1536.
- Wang, C., and D. B. Enfield, 2003: A further study of the tropical Western Hemisphere warm pool. *J. Climate*, **16**, 1476-1493.
- Wang, C., D. B. Enfield, S.-K. Lee, and C. W. Landsea, 2006: Influences of the Atlantic warm pool on Western Hemisphere summer rainfall and Atlantic hurricanes. *J. Climate*, **19**, 3011-3028.

- Wang, C., S.-K. Lee, and D. B. Enfield, 2007: Impact of the Atlantic warm pool on the summer climate of the Western Hemisphere. *J. Climate*, **20**, 5021-5040.
- Wang, C., S.-K. Lee, and D. B. Enfield, 2008a: Climate response to anomalously large and small Atlantic warm pools during the summer. *J. Climate*, **21**, 2437–2450.
- Wang, C., S.-K. Lee, and D. B. Enfield, 2008b: Atlantic warm pool acting as a link between Atlantic multidecadal oscillation and Atlantic tropical cyclone activity. *Geochem. Geophys. Geosyst.*, **9**, Q05V03, doi:10.1029/2007GC001809. (In the special issue of "Interactions between climate and tropical cyclones on all timescales".)
- Wang, Y. , S.-P. Xie, H. Xu, and B. Wang, 2004: Regional model simulations of marine boundary-layer clouds over the Southeast Pacific off South America. Part I: Control experiment. *Mon. Wea. Rev.*, **132** (1), 274–296.
- Webster, P. J., and R. Lukas, 1992: The Tropical Ocean/Global Atmosphere Coupled Ocean-atmosphere Response Experiment (COARE). *Bull. Amer. Meteor. Soc.*, **73**, 1377-1416.
- Yu, J. -Y., and C. R. Mechoso, 1999: Links between annual variations of Peruvian stratocumulus clouds and of SST in the eastern equatorial Pacific. *J. Climate*, **23**, 305-318.
- Zebiak, S. E., 1986: Atmospheric convergence feedback in a simple model for El Niño. *Mon. Wea. Rev.*, **114**, 1263-1271.

## Figure Captions

**Figure 1.** SST ( $^{\circ}\text{C}$ ) distribution in the AWP region during the four seasons. Shown are the SSTs in (a) the winter from December to February (DJF), (b) the spring from March to May (MAM), (c) the summer from June to August (JJA), and (d) the fall from September to November (SON). The contour interval is  $1.0^{\circ}\text{C}$ . The AWP box is marked. The box is used as the AWP region to force CAM3 with the large and small AWP composites of SST.

**Figure 2.** Velocity potential ( $10^6 \text{ m}^2/\text{s}$ ) and divergent wind ( $\text{m/s}$ ) at 200-mb from the NCEP-NCAR reanalysis. Shown are in (a) the winter from December to February (DJF), (b) the spring from March to May (MAM), (c) the summer from June to August (JJA), and (d) the fall from September to November (SON). The negative velocity potential is shaded and the contour interval is  $2.0 \times 10^6 \text{ m}^2/\text{s}$ .

**Figure 3.** The composite difference between the large and small AWP years for velocity potential ( $10^6 \text{ m}^2/\text{s}$ ) and divergent wind ( $\text{m/s}$ ) at 200-mb in (a) June to August (JJA) and (b) September to November (SON). The negative velocity potential difference is shaded and the contour interval is  $0.4 \times 10^6 \text{ m}^2/\text{s}$ . The composites are calculated from the NCEP-NCAR reanalysis. An AWP 25% larger (smaller) than the climatological AWP area is identified as a large (small) AWP; otherwise, AWP is classified as normal or neutral.

**Figure 4.** Velocity potential ( $10^6 \text{ m}^2/\text{s}$ ) and divergent wind ( $\text{m/s}$ ) at 200-mb from the CAM3 CTRL run. Shown are in (a) the winter from December to February (DJF), (b) the spring from

March to May (MAM), (c) the summer from June to August (JJA), and (d) the fall from September to November (SON). The negative velocity potential is shaded and the contour interval is  $2.0 \times 10^6 \text{ m}^2/\text{s}$ .

**Figure 5.** The 200-mb velocity potential ( $10^6 \text{ m}^2/\text{s}$ ) and divergent wind (m/s) difference between the LAWP and SAWP CAM3 ensemble runs in (a) June to August (JJA) and (b) September to November (SON). The negative velocity potential difference is shaded and the contour interval is  $0.5 \times 10^6 \text{ m}^2/\text{s}$ .

**Figure 6.** The zonal-vertical sections of vertical pressure velocity ( $10^{-2} \text{ Pa/s}$ ) and meridional wind (m/s) at  $25^\circ\text{S}$  in JJA from CAM3 model runs. Shown are (a) the vertical pressure velocity and (c) meridional wind from the CTRL run, (b) the vertical pressure velocity and (d) meridional wind difference between the LAWP and SAWP CAM3 ensemble runs. The positive vertical pressure velocity is shaded. The contour intervals in (a), (b), (c) and (d) are  $1.0 \times 10^{-2} \text{ Pa/s}$ ,  $0.2 \times 10^{-2} \text{ Pa/s}$ , 1.0 m/s and 0.2 m/s, respectively. The unit on the vertical axis is hPa.

**Figure 7.** The zonal-vertical sections of vertical pressure velocity ( $10^{-2} \text{ Pa/s}$ ) and meridional wind (m/s) at  $25^\circ\text{S}$  in SON from CAM3 model runs. Shown are (a) the vertical pressure velocity and (c) meridional wind from the CTRL run, (b) the vertical pressure velocity and (d) meridional wind difference between the LAWP and SAWP CAM3 ensemble runs. The positive vertical pressure velocity is shaded. The contour intervals in (a), (b), (c) and (d) are  $1.0 \times 10^{-2} \text{ Pa/s}$ ,  $0.4 \times 10^{-2} \text{ Pa/s}$ , 1.0 m/s and 0.4 m/s, respectively. The unit on the vertical axis is hPa.

**Figure 8.** The baroclinic and barotropic stream function ( $10^7 \text{ m}^2/\text{s}$ ) difference between the LAWP and SAWP CAM3 ensemble runs. Shown are (a) the baroclinic stream function in JJA, (b) the barotropic stream function in JJA, (c) the baroclinic stream function in SON, and (d) the barotropic stream function in SON. The negative stream function is shaded. The contour interval in (a) and (c) is  $0.1 \times 10^7 \text{ m}^2/\text{s}$  and the contour interval in (b) and (d) is  $0.05 \times 10^7 \text{ m}^2/\text{s}$ .

**Figure 9.** The stream function ( $10^7 \text{ m}^2/\text{s}$ ) difference between the LAWP and SAWP CAM3 ensemble runs. Shown are (a) the stream function at 750-mb in JJA, (b) the stream function at 250-mb in JJA, (c) the stream function at 750-mb in SON, and (d) the stream function at 250-mb in SON. The negative stream function is shaded and the contour interval is  $0.1 \times 10^7 \text{ m}^2/\text{s}$ .

**Figure 10.** The background mean zonal winds (m/s) from the NCEP-NCAR reanalysis in JJA and SON. Shown are (a) the background vertical zonal wind shear  $-\hat{U}$  and (b) the background vertical zonal wind mean  $\bar{U}$ . The background mean states are calculated by the zonal average between  $120^\circ\text{W}$ - $40^\circ\text{W}$  as  $\hat{U} = (U_{750\text{mb}} - U_{250\text{mb}}) / 2$  and  $\bar{U} = (U_{750\text{mb}} + U_{250\text{mb}}) / 2$ .

**Figure 11.** Stream functions ( $10^7 \text{ m}^2/\text{s}$ ) of the (a) baroclinic and (b) barotropic components in JJA from the simple model. The negative stream function is shaded. The contour interval in (a) is  $0.25 \times 10^7 \text{ m}^2/\text{s}$  and the contour interval in (b) is  $0.05 \times 10^7 \text{ m}^2/\text{s}$ .

**Figure 12.** Stream functions ( $10^7 \text{ m}^2/\text{s}$ ) of the (a) baroclinic and (b) barotropic components in SON from the simple model. The negative stream function is shaded. The contour interval in (a) is  $0.25 \times 10^7 \text{ m}^2/\text{s}$  and the contour interval in (b) is  $0.05 \times 10^7 \text{ m}^2/\text{s}$ .

**Figure 13.** Stream functions ( $10^7 \text{ m}^2/\text{s}$ ) of the (a) baroclinic and (b) barotropic components in JJA from the simple model run:  $\hat{U} = 0$  (without the background vertical wind shear) over the Southern Hemisphere. The negative stream function is shaded. The contour interval in (a) is  $0.25 \times 10^7 \text{ m}^2/\text{s}$  and the contour interval in (b) is  $0.05 \times 10^7 \text{ m}^2/\text{s}$ .

**Figure 14.** Stream functions ( $10^7 \text{ m}^2/\text{s}$ ) of the (a) baroclinic and (b) barotropic components in JJA from the simple model run:  $\bar{U} = 0$  (without the background vertical wind mean) over the Southern Hemisphere. The negative stream function is shaded. The contour interval in (a) is  $0.25 \times 10^7 \text{ m}^2/\text{s}$  and the contour interval in (b) is  $0.05 \times 10^7 \text{ m}^2/\text{s}$ .

## HADISST: Sea Surface Temperature

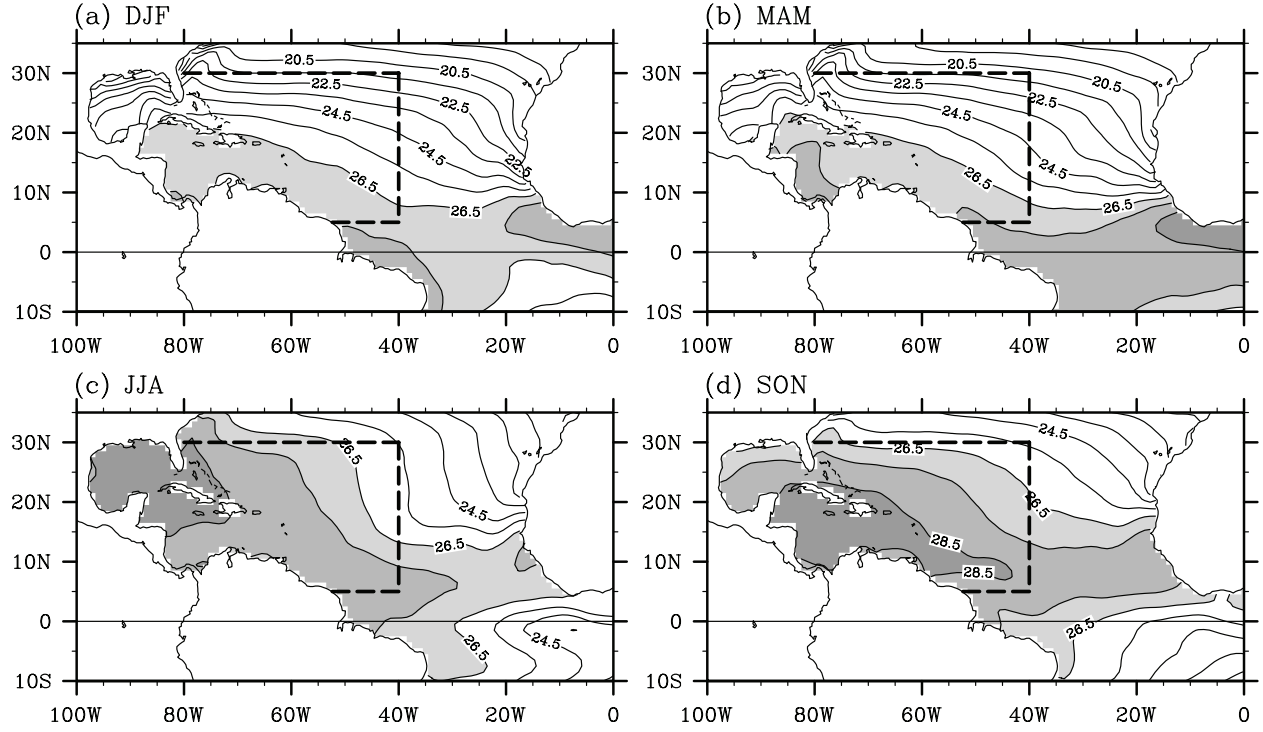


**Figure 1.** SST ( $^{\circ}\text{C}$ ) distribution in the AWP region during the four seasons. Shown are the SSTs in (a) the winter from December to February (DJF), (b) the spring from March to May (MAM), (c) the summer from June to August (JJA), and (d) the fall from September to November (SON). The contour interval is  $1.0^{\circ}\text{C}$ . The AWP box is marked. The box is used as the AWP region to force CAM3 with the large and small AWP composites of SST.

NCEP1: VPOT and Divergent Wind at 200 hPa

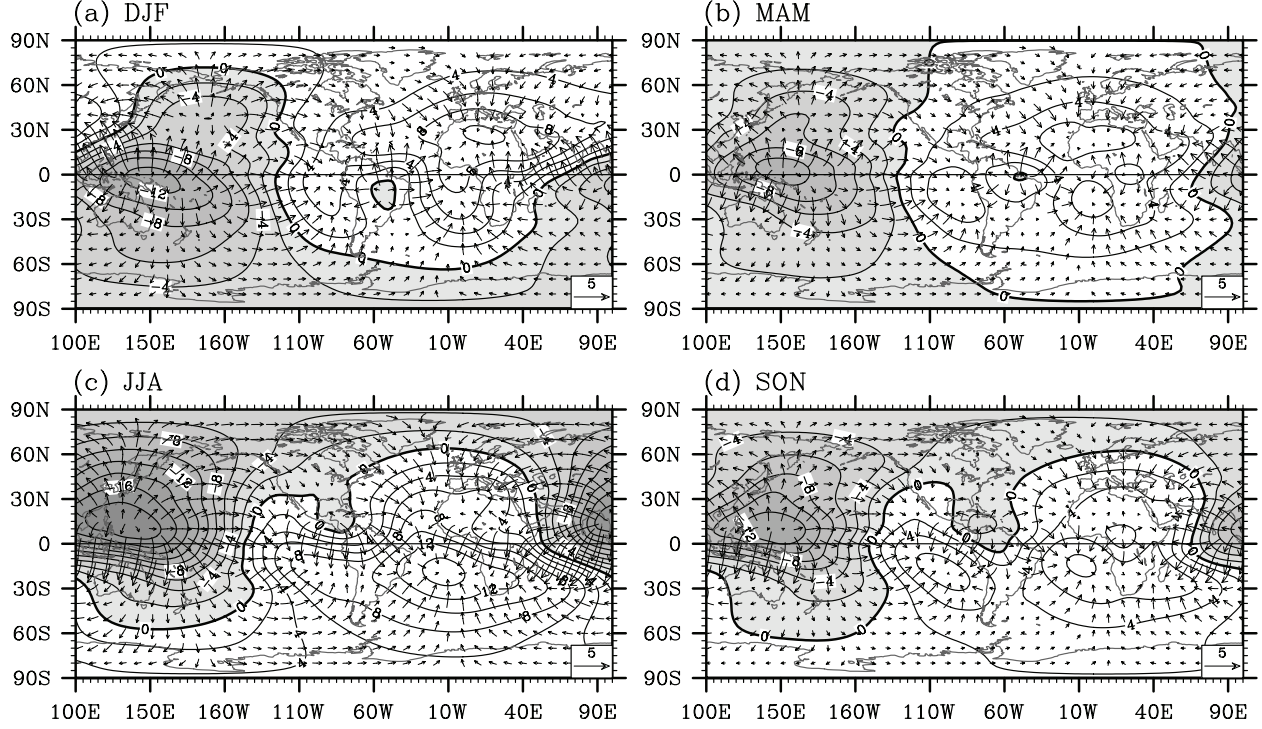


**Figure 2.** Velocity potential ( $10^6 \text{ m}^2/\text{s}$ ) and divergent wind (m/s) at 200-mb from the NCEP-NCAR reanalysis. Shown are in (a) the winter from December to February (DJF), (b) the spring from March to May (MAM), (c) the summer from June to August (JJA), and (d) the fall from September to November (SON). The negative velocity potential is shaded and the contour interval is  $2.0 \times 10^6 \text{ m}^2/\text{s}$ .



NCEP1: VPOT and Div. Wind at 200 hPa

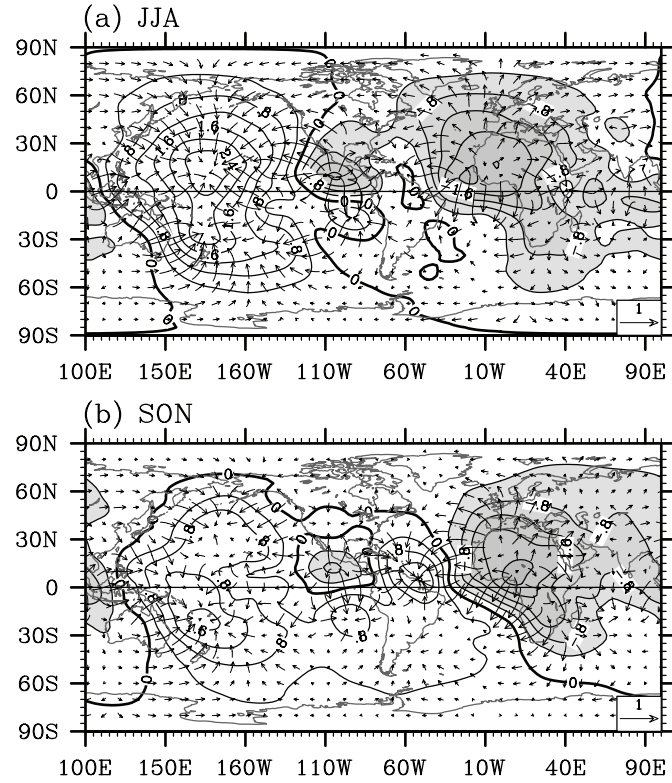


**Figure 3.** The composite difference between the large and small AWP years for velocity potential ( $10^6 \text{ m}^2/\text{s}$ ) and divergent wind (m/s) at 200-mb in (a) June to August (JJA) and (b) September to November (SON). The negative velocity potential difference is shaded and the contour interval is  $0.4 \times 10^6 \text{ m}^2/\text{s}$ . The composites are calculated from the NCEP-NCAR reanalysis. An AWP 25% larger (smaller) than the climatological AWP area is identified as a large (small) AWP; otherwise, AWP is classified as normal or neutral.

CAM3 CTRL: VPOT and Divergent Wind at 200 hPa

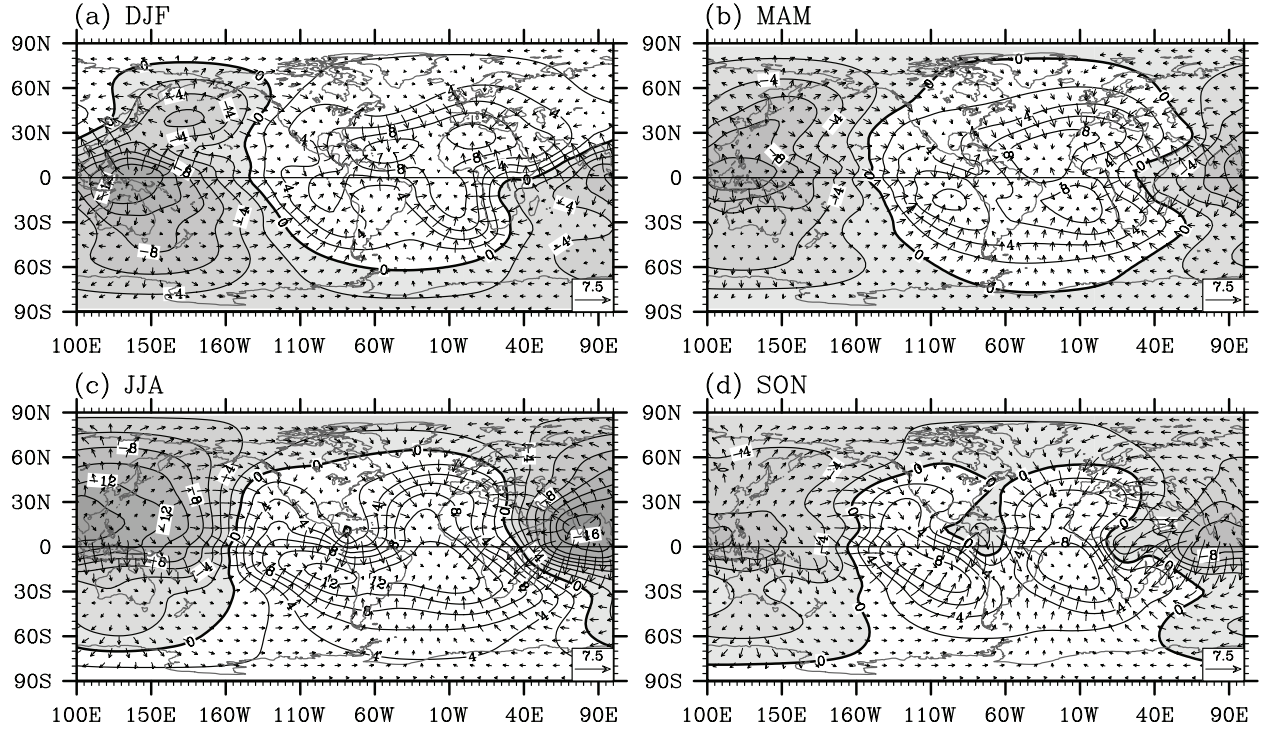


**Figure 4.** Velocity potential ( $10^6 \text{ m}^2/\text{s}$ ) and divergent wind ( $\text{m/s}$ ) at 200-mb from the CAM3 CTRL run. Shown are in (a) the winter from December to February (DJF), (b) the spring from March to May (MAM), (c) the summer from June to August (JJA), and (d) the fall from September to November (SON). The negative velocity potential is shaded and the contour interval is  $2.0 \times 10^6 \text{ m}^2/\text{s}$ .

# CAM3 (LAWP-SWAP)

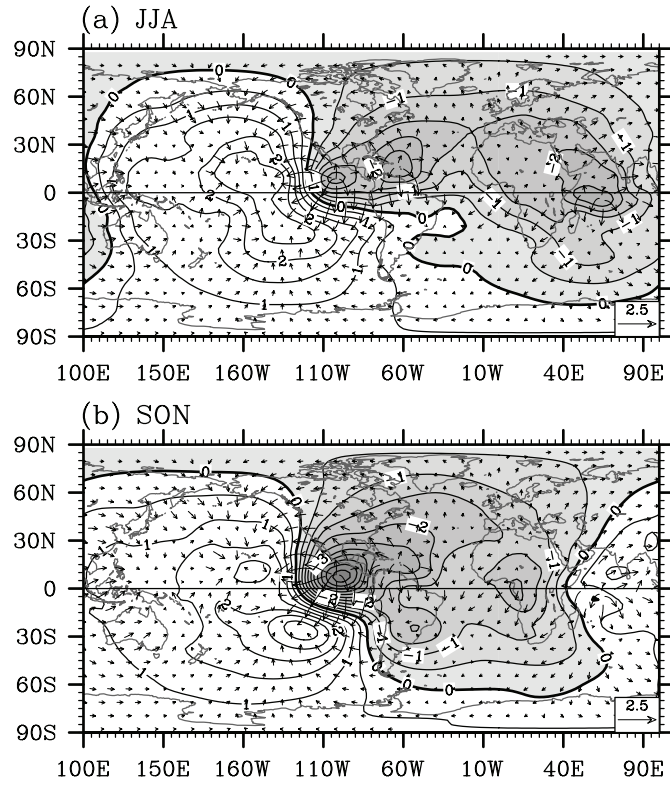


**Figure 5.** The 200-mb velocity potential ( $10^6 \text{ m}^2/\text{s}$ ) and divergent wind ( $\text{m/s}$ ) difference between the LAW and SWAP CAM3 ensemble runs in (a) June to August (JJA) and (b) September to November (SON). The negative velocity potential difference is shaded and the contour interval is  $0.5 \times 10^6 \text{ m}^2/\text{s}$ .

CAM3: Vertical Pressure Velocity and Meridional Wind at 25S (JJA)

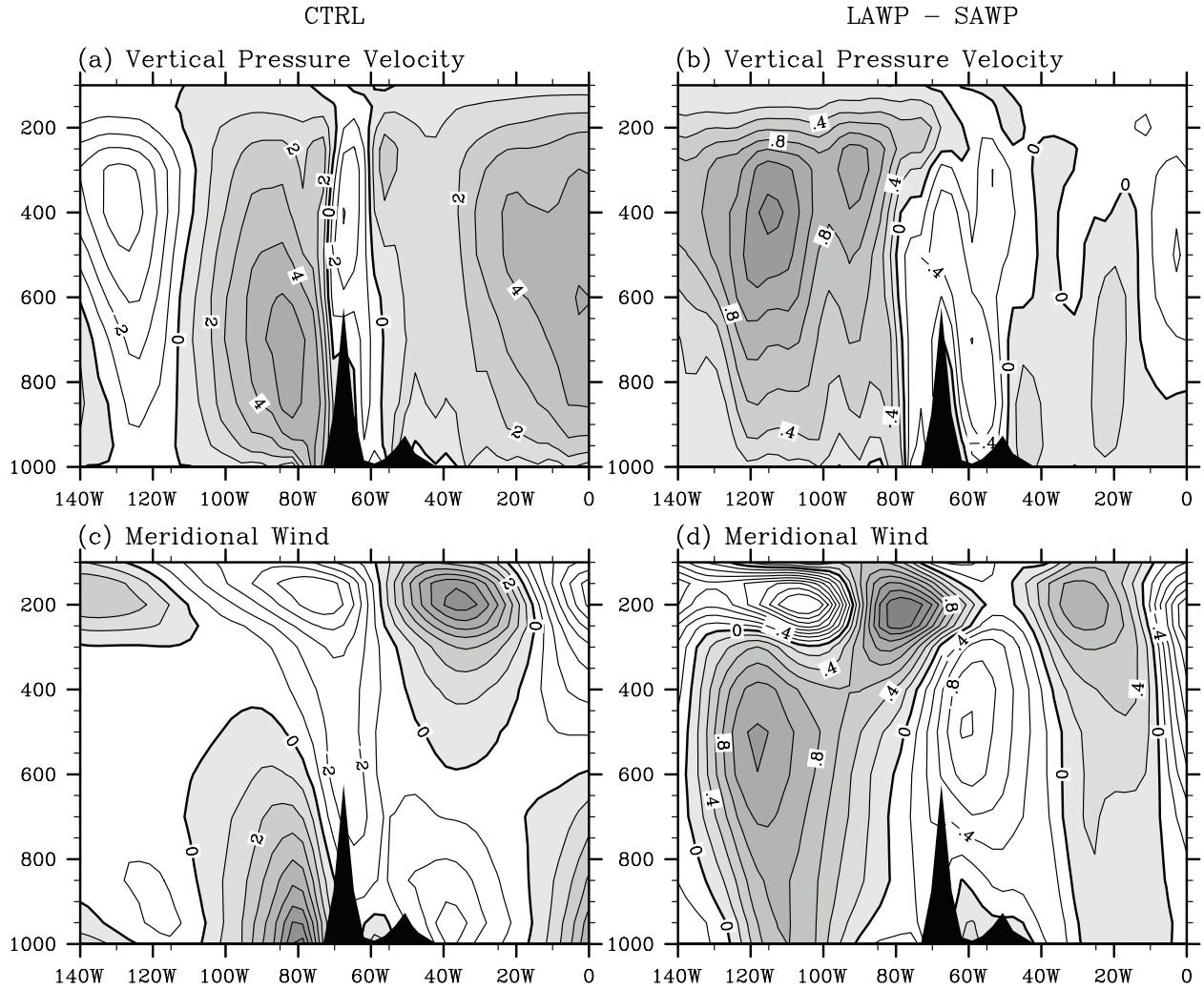


**Figure 6.** The zonal-vertical sections of vertical pressure velocity ( $10^{-2}$  Pa/s) and meridional wind (m/s) at 25°S in JJA from CAM3 model runs. Shown are (a) the vertical pressure velocity and (c) meridional wind from the CTRL run, (b) the vertical pressure velocity and (d) meridional wind difference between the LAWP and SAWP CAM3 ensemble runs. The positive vertical pressure velocity is shaded. The contour intervals in (a), (b), (c) and (d) are  $1.0 \times 10^{-2}$  Pa/s,  $0.2 \times 10^{-2}$  Pa/s, 1.0 m/s and 0.2 m/s, respectively. The unit on the vertical axis is hPa.

CAM3: Vertical Pressure Velocity and Meridional Wind at 25S (SON)

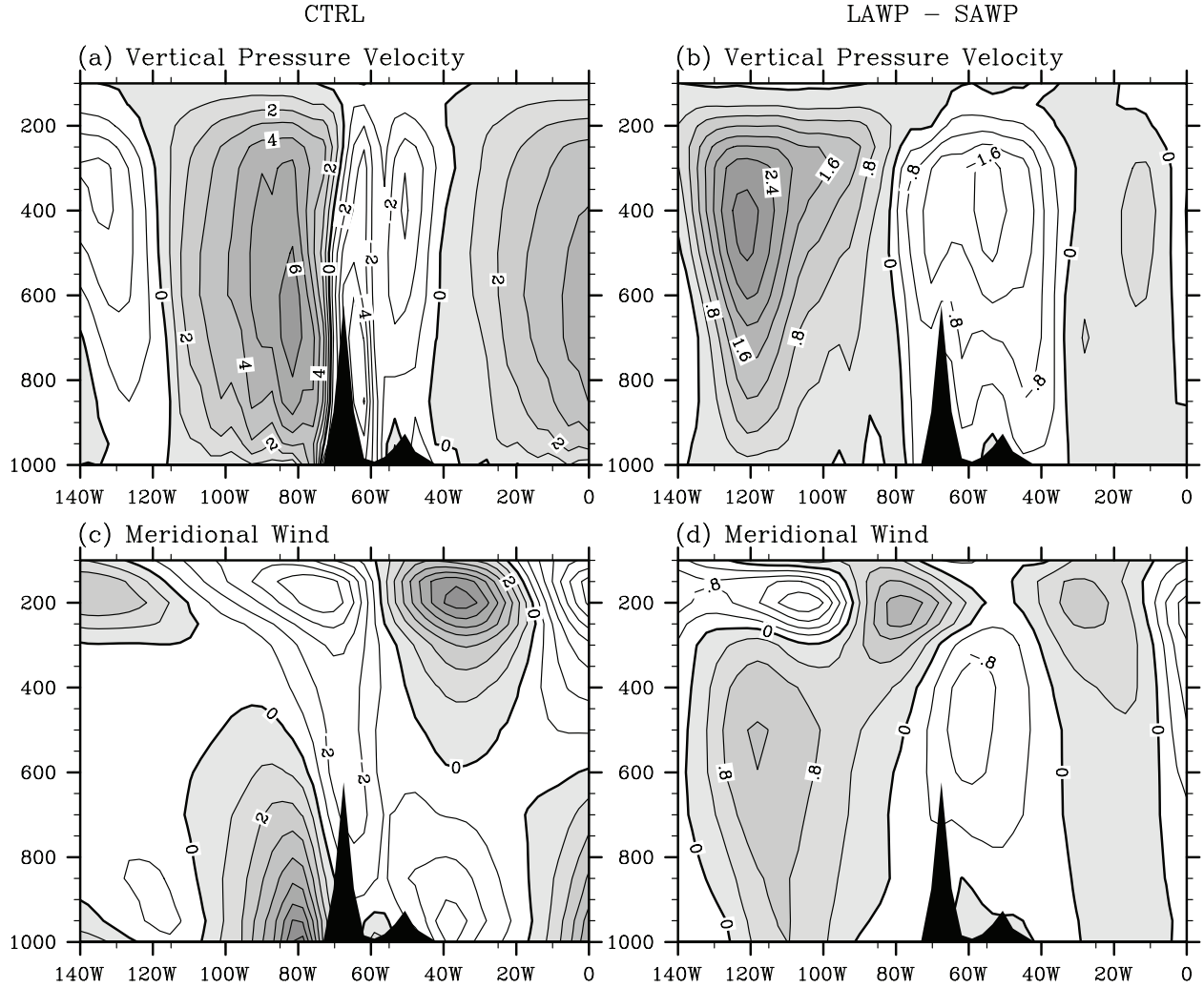


**Figure 7.** The zonal-vertical sections of vertical pressure velocity ( $10^{-2}$  Pa/s) and meridional wind (m/s) at 25°S in SON from CAM3 model runs. Shown are (a) the vertical pressure velocity and (c) meridional wind from the CTRL run, (b) the vertical pressure velocity and (d) meridional wind difference between the LAW and SAWP CAM3 ensemble runs. The positive vertical pressure velocity is shaded. The contour intervals in (a), (b), (c) and (d) are  $1.0 \times 10^{-2}$  Pa/s,  $0.4 \times 10^{-2}$  Pa/s, 1.0 m/s and 0.4 m/s, respectively. The unit on the vertical axis is hPa.

CAM3 (LAWP – SAWP)

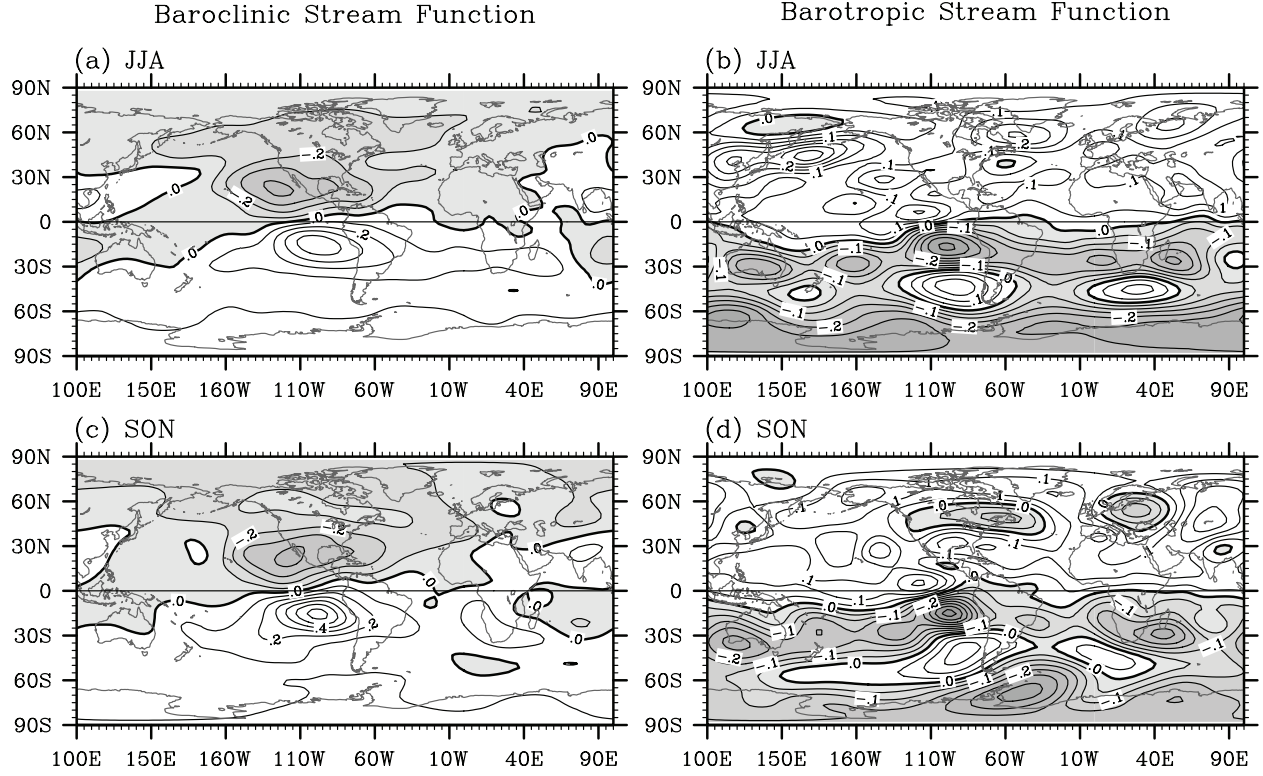


**Figure 8.** The baroclinic and barotropic stream function ( $10^7 \text{ m}^2/\text{s}$ ) difference between the LAWP and SAWP CAM3 ensemble runs. Shown are (a) the baroclinic stream function in JJA, (b) the barotropic stream function in JJA, (c) the baroclinic stream function in SON, and (d) the barotropic stream function in SON. The negative stream function is shaded. The contour interval in (a) and (c) is  $0.1 \times 10^7 \text{ m}^2/\text{s}$  and the contour interval in (b) and (d) is  $0.05 \times 10^7 \text{ m}^2/\text{s}$ .



CAM3 (LAWP - SAWP)

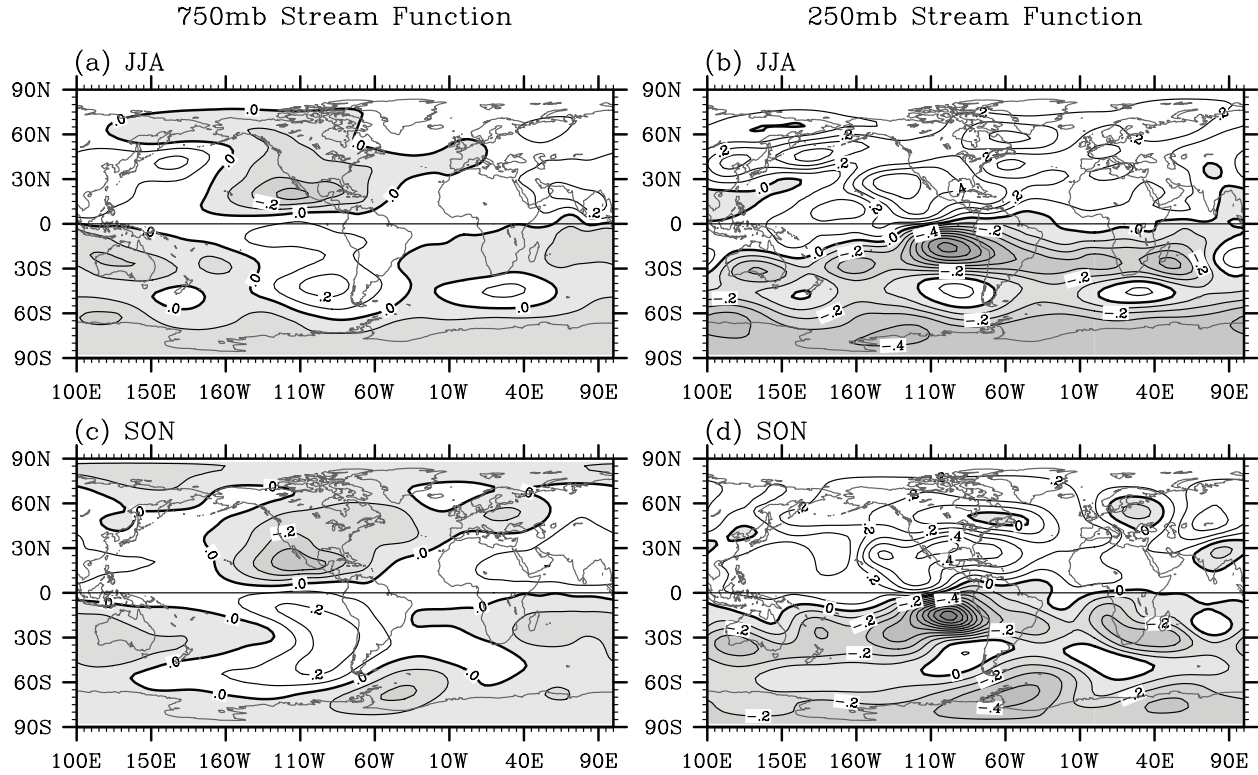


**Figure 9.** The stream function ( $10^7$  m<sup>2</sup>/s) difference between the LAWP and SAWP CAM3 ensemble runs. Shown are (a) the stream function at 750-mb in JJA, (b) the stream function at 250-mb in JJA, (c) the stream function at 750-mb in SON, and (d) the stream function at 250-mb in SON. The negative stream function is shaded and the contour interval is  $0.1 \times 10^7$  m<sup>2</sup>/s.

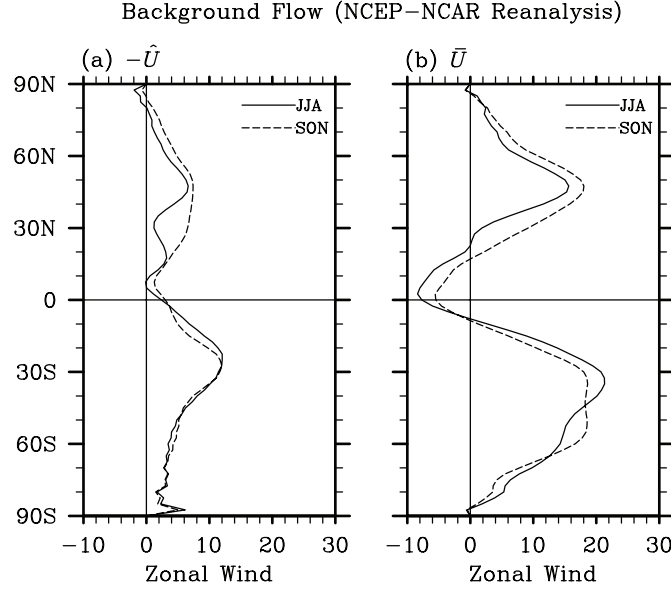


**Figure 10.** The background mean zonal winds (m/s) from the NCEP-NCAR reanalysis in JJA and SON. Shown are (a) the background vertical zonal wind shear  $-\hat{U}$  and (b) the background vertical zonal wind mean  $\bar{U}$ . The background mean states are calculated by the zonal average between 120°W-40°W as  $\hat{U} = (U_{750mb} - U_{250mb}) / 2$  and  $\bar{U} = (U_{750mb} + U_{250mb}) / 2$ .



# Simple Model (JJA)

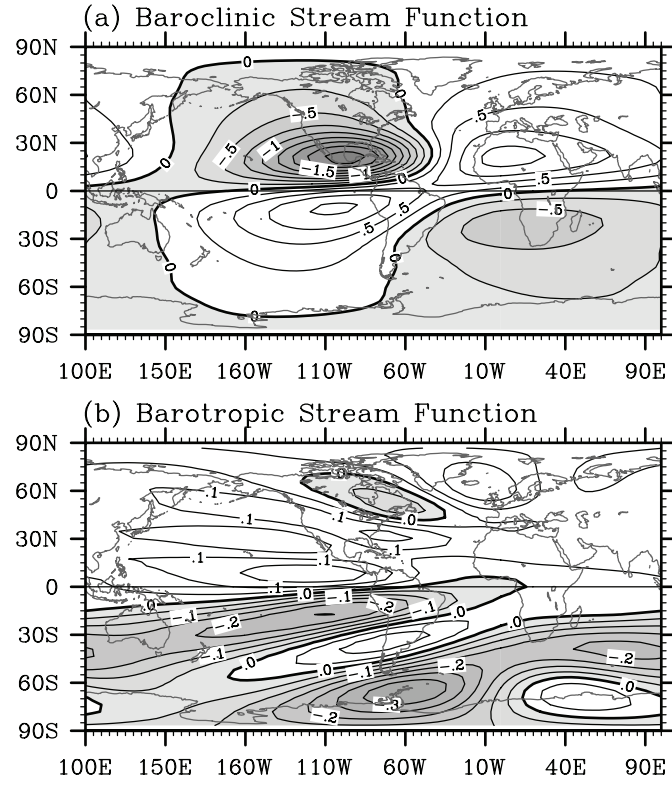


**Figure 11.** Stream functions ( $10^7 \text{ m}^2/\text{s}$ ) of the (a) baroclinic and (b) barotropic components in JJA from the simple model. The negative stream function is shaded. The contour interval in (a) is  $0.25 \times 10^7 \text{ m}^2/\text{s}$  and the contour interval in (b) is  $0.05 \times 10^7 \text{ m}^2/\text{s}$ .

## Simple Model (SON)

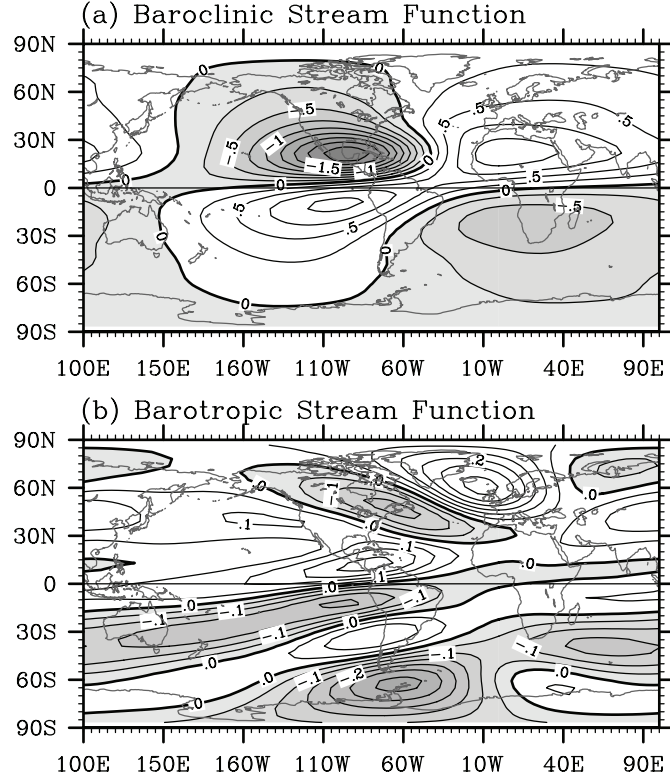


**Figure 12.** Stream functions ( $10^7 \text{ m}^2/\text{s}$ ) of the (a) baroclinic and (b) barotropic components in SON from the simple model. The negative stream function is shaded. The contour interval in (a) is  $0.25 \times 10^7 \text{ m}^2/\text{s}$  and the contour interval in (b) is  $0.05 \times 10^7 \text{ m}^2/\text{s}$ .

# Simple Model (JJA)

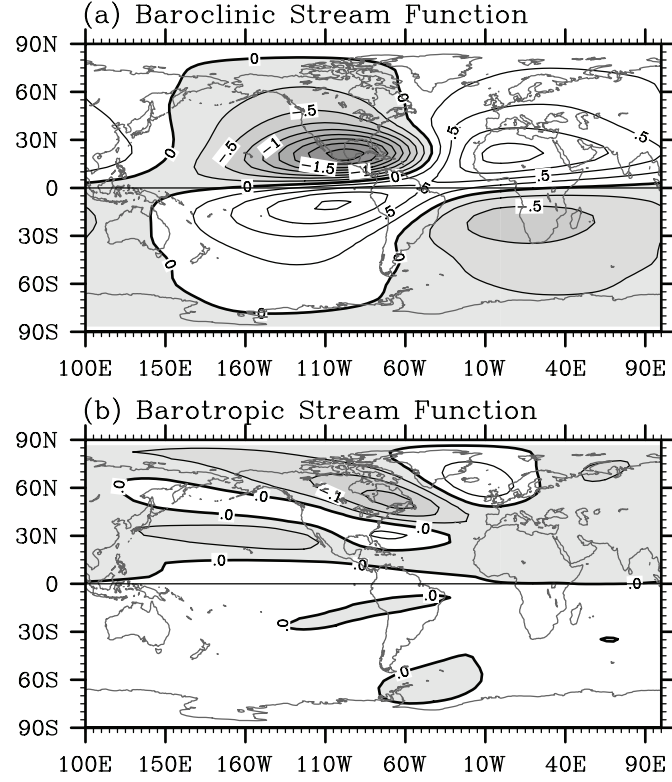


**Figure 13.** Stream functions ( $10^7 \text{ m}^2/\text{s}$ ) of the (a) baroclinic and (b) barotropic components in JJA from the simple model run:  $\hat{U} = 0$  (without the background vertical wind shear) over the Southern Hemisphere. The negative stream function is shaded. The contour interval in (a) is  $0.25 \times 10^7 \text{ m}^2/\text{s}$  and the contour interval in (b) is  $0.05 \times 10^7 \text{ m}^2/\text{s}$ .

# Simple Model (JJA)

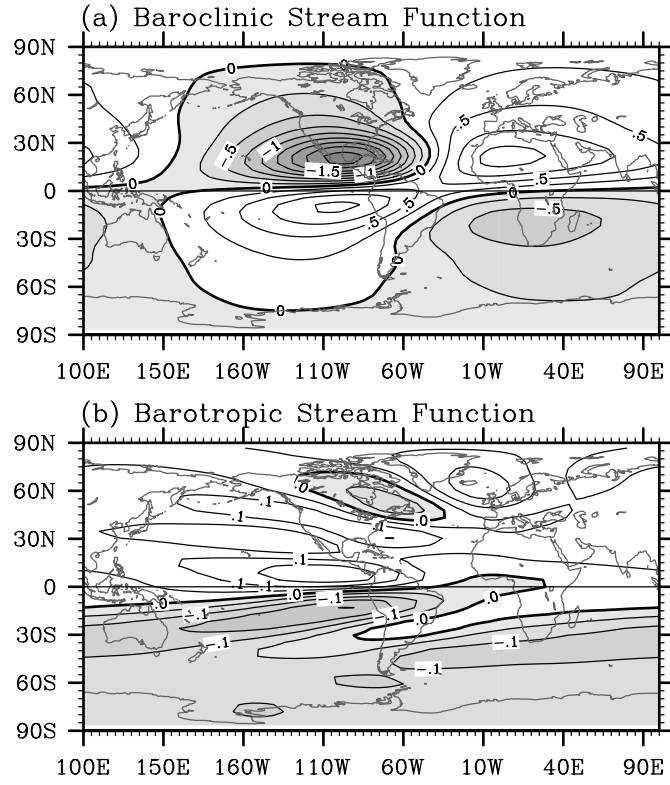


**Figure 14.** Stream functions ( $10^7 \text{ m}^2/\text{s}$ ) of the (a) baroclinic and (b) barotropic components in JJA from the simple model run:  $\bar{U} = 0$  (without the background vertical wind mean) over the Southern Hemisphere. The negative stream function is shaded. The contour interval in (a) is  $0.25 \times 10^7 \text{ m}^2/\text{s}$  and the contour interval in (b) is  $0.05 \times 10^7 \text{ m}^2/\text{s}$ .